

Cross-Path LIDAR for Turbulence Profile Determination

Mikhail S. Belen'kii

Trex Enterprises Corporation

10455 Pacific Center Court San Diego, CA 92121

Don Bruns

Trex Enterprises Corporation

10455 Pacific Center Court San Diego, CA 92121

Kevin A. Hughes

Trex Enterprises Corporation

10455 Pacific Center Court San Diego, CA 92121

Vincent A. Rye

Trex Enterprises Corporation

10455 Pacific Center Court San Diego, CA 92121

Frank Eaton

Air Force Research Laboratory, Directed Energy Directorate

3550 Aberdeen Ave SE, Kirtland AFB, NM 87117

ABSTRACT

Knowledge of the turbulence profile is important for various applications including directed energy systems such as Airborne Laser and Tactical Airborne Laser, ground-based adaptive optics telescopes, and laser communication systems. The known methods for turbulence profile determination have various limitations. We present a concept of a cross-path LIDAR that overcomes these shortcomings. Our sensor system uses laser guide star technology combined with a cross-path wavefront sensing technique. This sensor has several advantages as compared with the known approaches. A cross-path LIDAR has high spatial and temporal resolution, can operate along arbitrary atmospheric paths in the presence of strong turbulence both at daytime and night, and does not depend on the availability of binary stars. We evaluated the feasibility of this approach by carrying out a performance and error budget analysis, developing an analytical model for the wavefront slope cross-correlation and validating this model using wave optics code, examining the sensitivity of the wavefront slope cross-correlation to the variations of the turbulence profile, and developing and testing an inversion algorithm for reconstruction of the turbulence profile from the optical measurements, as well as developing conceptual LIDAR design. The performed study confirmed that the cross-path LIDAR is feasible.

Keywords: turbulence, remote sensing, wavefront sensor, inversion algorithm,

1. INTRODUCTION

Random variations of the index of refraction called refractive turbulence degrade images and laser beams propagating in the atmosphere. Thus turbulence degrades the performance of various imaging and laser projection systems. High bandwidth tracking and adaptive optics (AO) systems can compensate for the effects of turbulence. However, in order to understand the results of the imaging, or laser propagation, field tests with AO systems, knowledge of the distribution of the strength of turbulence along the propagation path is required. Accurate measurements of the turbulence profile are also required to improve the performance of adaptive optics systems designed to compensate the effects of turbulence on directed energy and laser communication systems. The correspondent optical sensor must have high spatial and temporal resolution, be independent of availability of binary stars, be able to operate in the presence of strong turbulence, and sense turbulence from ground-to-space, between two points on the ground, and from an aircraft to the ground, or to another aircraft.

Several methods for turbulence profile determination, including temperature probes [1, 2], differential image motion (DIM) sensor [3], scintillation detection and ranging (SCIDAR) sensor [4-6], differential image motion (DIM) LIDAR [7], and slope detection and ranging (SLODAR) sensor [8] are known. However, they have various limitations. In particular:

- in-situ measurements using temperature probes [1,2] are not possible in many situations
- DIM sensor [3] provides only path-integrated information. It measures Fried parameter, r_0 , not the turbulence profile
- the SCIDAR [4-6] is based on scintillation measurements. It is limited by availability of bright binary stars and can operate exclusively in weak scintillation regime
- a DIM LIDAR [7] sequentially probes the atmosphere at different locations along the path. Consequently, it has limited temporal resolution.
- a SLODAR [8] depends on availability of binary stars. It does not allow us to measure turbulence from a moving platform.

We introduced and evaluated a feasibility of a concept of a cross-path LIDAR that overcomes the above shortcomings. Similar to that in approach [9] a cross-path LIDAR uses a pulsed laser, a wavefront sensor, and a range-gated camera. According to this concept, two laser beacons are created at a fixed range and at some angular distance from each other using a pulsed laser. The wavefront slopes of the laser the return from each beacon are measured with a wavefront sensor. Time and space averaged cross-correlations of the wavefront slopes are calculated. A turbulence profile of refractive index structure characteristics $C_n^2(z)$ is reconstructed from the measured cross-correlations of the wavefront slopes by inverting the corresponding integral equation.

2. CROSS-PATH LIDAR CONCEPT

The cross-path LIDAR concept is the following schematically in Figure 1. Two laser guide stars (LGSs) separated at angular distance θ are created at the fixed measurement range using a pulsed laser. The wavefront slopes of a laser return from each LGS are measured with a Hartmann wavefront sensor having $n_{sub} = D/D_{sub}$ sub-apertures, where D is the telescope aperture diameter, D_{sub} is the sub-aperture diameter, and a range-gated camera.

For a binary LGS with angular separation θ a single turbulent layer at altitude H produces two “copies” of the aberrated wavefront in the pupil plane of the telescope, shifted by distance $S = H\theta$ with respect to one another. Consequently, the cross-correlation of the wavefront slopes has a peak at baseline separation S in the direction of the binary separation. The amplitude of the peak of the wavefront slope cross-correlation at the separation S depends on the strength of turbulence of the turbulent layer located at the altitude H where two optical paths are crossed

$$H = S / \theta \quad (1)$$

The thickness of the layer is determined by the sub-aperture diameter divided by the angular separation

$$\delta H = D_{sub} / \theta \quad (2)$$

This value defines the spatial resolution of the cross-path LIDAR technique. As shown in Figure 1, each pair of sub-apertures separated at distance r_i , $i = 1, \dots, n_{sub}$ in the direction of the binary LGSs separation “samples” atmospheric turbulence within the layer located at the altitude $H_i = r_i / \theta$. For a 3.5 m diameter telescope and sub-aperture diameter of $D_{sub} = 0.15$ m, the number of sampled turbulent layers is $n_{sub} = 23$, whereas a 1 m diameter telescope and $D_{sub} = 0.1$ m, this number is $n_{sub} = 10$.

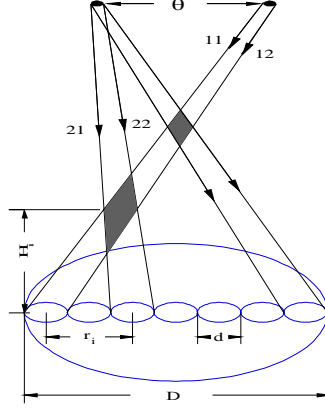


Fig. 1. Schematic of the cross-path LIDAR technique using two LGSs and a Hartmann wavefront sensor.

A cross-path LIDAR has several advantages. As opposed to the Differential Image Motion (DIM) LIDAR⁷, which uses a single LGS and two spatially separated sub-apertures to perform sequential measurements of the wavefront slope statistics at altitudes H_i , a cross path LIDAR samples the atmospheric turbulence at all altitudes H_i , $i = 1, \dots, n_{sub}$ simultaneously. This significantly increases a temporal resolution. For example, to achieve a good statistical accuracy for the wavefront slope measurements, the data acquired at each altitude H_i should be averaged during 60-120 sec using both techniques. The implication is that it will take 25-50 min to measure the turbulence profile at 25 altitudes using DIM LIDAR [7], whereas it will take 60-120 sec to measure the same profile using cross-path LIDAR technique.

Other advantages of a cross-path LIDAR, as compared to the known techniques [1-8], include:

- high spatial resolution due to the use of multiple sub-apertures of a wavefront sensor that sample turbulence at different locations along the path. The number of layers is determined by the number of sub-apertures of the wavefront sensor. The thickness of the turbulent layers is determined by the ratio of the sub-aperture diameter to the angular distance between the laser beacons given by Eq. (2)
- the cross-path LIDAR can operate along arbitrary atmospheric paths including regime of strong scintillation because this method is based on phase related phenomenon, and it does not saturate with increasing the strength of turbulence and/or range
- the cross-path LIDAR is independent of the availability of binary stars, it can measure turbulence characteristics from ground to space, between two points on the ground, and from an aircraft
- the LIDAR can operate using various optical sources: Rayleigh beacons, sodium laser guide stars (LGSs) and natural stars.

To validate the feasibility of this method, we developed an analytical model for the cross-correlation of the wavefront slopes of laser returns from two LGSs, evaluated the sensitivity of the slope cross-correlation to the turbulence profile $C_n^2(z)$ variations, c) developed and tested an inversion algorithm for reconstruction of the turbulence profile from optical measurements, carried out a performance analysis, determined design requirements, and developed a conceptual design for the cross-path LIDAR. In addition, we developed an optimal design of a sodium atomic line filter for daytime operation of cross-path LIDAR using sodium LGSs [10].

3. ANALYTICAL MODEL FOR CROSS-PATH LIDAR

First, we will examine an analytical model for an astronomical scenario using two binary stars. We assume that two plane waves from binary stars separated at angular distance θ propagate down through the atmosphere. The optical

rays of the two waves that arrive at two sub-apertures, separated at the distance r_i in the direction of the binary stars separation, are crossed at the altitude $H_i = r_i / \theta$ (see. Fig.1). In geometrical optics approximation the phase difference between two optical rays arriving at the i^{th} sub-aperture having diameter d has the form [11]

$$\delta_i = \phi(x_{2,i}) - \phi(x_{1,i}) = k \int_0^{H_{\max}} dz \{n[p_{2,i}(z)] - n[p_{1,i}(z)]\} \quad (3)$$

where k is the wave number, and $n[p(z)]$ is the refractive index along the optical ray. The cross-correlation of the wave front slopes is expressed through the combination of the phase structure functions

$$\langle \delta_1 \delta_2 \rangle = D_s(\vec{r}_i - \vec{d}, \vec{\theta}) + D_s(\vec{r}_i + \vec{d}, \vec{\theta}) - 2D_s(\vec{r}_i, \vec{\theta}) \quad (4)$$

where the phase structure function for Kolmogorov turbulence model and vertical propagation path is

$$D(\vec{\rho}_i, \theta) = 1.45k^2 \int_0^{H_{\max}} dz C_n^2(z) \left| (1 - z/L)\vec{\rho}_i - z\vec{\theta} \right|^{5/3} \quad (5)$$

Here $C_n^2(z)$ is the turbulence vertical profile, $\vec{\rho} = \vec{r}_i \pm \vec{d}$, and L is the distance of the LGS from the telescope. For natural guides stars, $L = \infty$. We will assume that both vectors \vec{r}_i and \vec{d} are parallel to the vector $\vec{\theta}$ of the separation between the LGSs. Consequently, an integral equation that relates the cross-correlation coefficient of the wavefront slopes to the turbulence profile has the form

$$b(r_i, \theta) = \int_0^{H_{\max}} C_n^2(z) W(r_i, \theta, z) dz \quad (6)$$

where $b(r_i, \theta)$ is the slope cross-correlation normalized to the slope variance $b(r_i, \theta) = \langle d_1 d_2 \rangle / \langle d^2 \rangle$, and $W(r_i, \theta, z)$ is the path weighting function. For natural guide stars the path-weighting function is

$$W(r_i, \theta, z) = \left[(r_i - D_{sub})^2 - 2z(r_i - D_{sub})\theta + (z\theta)^2 \right]^{5/6} + \left[(r_i + D_{sub})^2 - 2z(r_i + D_{sub})\theta + (z\theta)^2 \right]^{5/6} - 2 \left[r_i^2 - 2zr_i\theta + (z\theta)^2 \right]^{5/6} \quad (7)$$

Fig.2 shows the path weighting functions for binary stars. The path weighting function has multiple peaks at the altitudes where two optical paths are crossed. The number of peaks is determined by the number of sub apertures. For $D = 3.5$ m and $D_{sub} = 0.15$ m, $n_{sub} = 23$. It defines the number of sampled atmospheric layers.

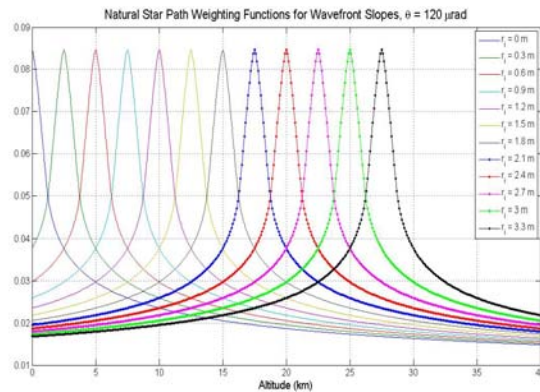


Fig. 2. The path weighting functions for the wavefront slopes for the natural guide star vs separation between the sub-apertures of a wavefront sensor. The telescope diameter $D = 3.5$ m, sub-aperture diameter $D_{sub} = 0.15$ m, and separation between the LGSs is $\theta = 120 \mu\text{rad}$.

Now, we consider the sodium LGSs located at 90 km altitude. In this case, the path-weighting function is given by

$$W(r_i, \theta, z) = \left[\left(1 - \frac{z}{F}\right)^2 (r_i - D_{sub})^2 - 2\left(1 - \frac{z}{F}\right)(r_i - D_{sub})z\theta + (z\theta)^2 \right]^{5/6} + \left[\left(1 - \frac{z}{F}\right)^2 (r_i + D_{sub})^2 - 2\left(1 - \frac{z}{F}\right)z(r_i + D_{sub})\theta + (z\theta)^2 \right]^{5/6} - 2 \left[\left(1 - \frac{z}{F}\right)^2 r_i^2 - 2\left(1 - \frac{z}{F}\right)zr_i\theta + (z\theta)^2 \right]^{5/6} \quad (8)$$

where F is the focal length of the laser beam, $F = 90km$. This path weighting function takes into account the spherical divergence of laser beacon waves. Figure 3a depicts the path weighting functions for sodium LGS at 90 km. The path weighting functions for Rayleigh LGS at 15 km altitude are shown in Figure 3b. The telescope aperture diameter is 1 m, and the sub-aperture diameter is $D_{sub} = 0.1$ m. The angular separation between the LGSs is $40\mu rad$, and the focal length of the laser beam is $F = 30km$. The cross-correlation coefficients have 10 peaks at different altitudes, where the corresponding optical paths are crossed, $H_i = r_i / \theta$.

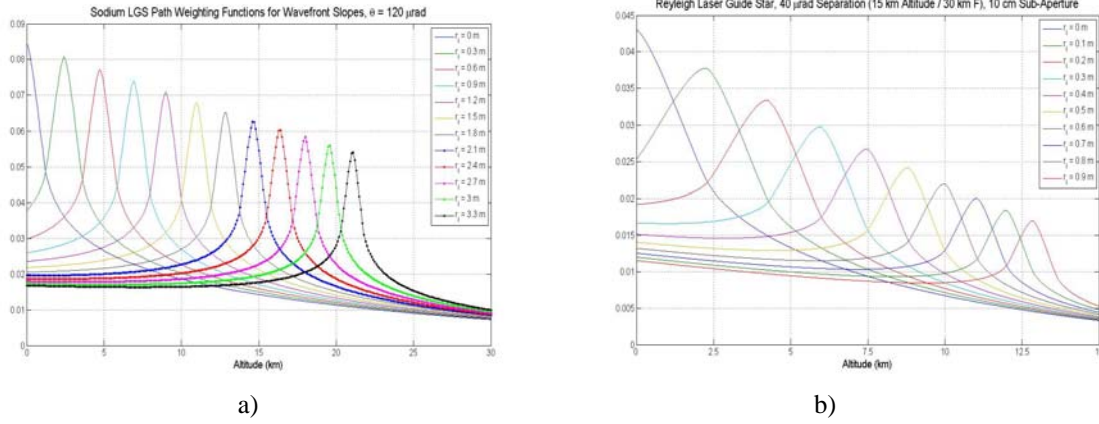


Fig. 3. Path weighting functions for the cross-correlation of the wavefront slopes for the sodium LGS at 90 km altitude (a) and Rayleigh LGS at 15 km altitude (b) vs. separation between the sub-apertures of a wavefront sensor. For sodium beacons, the telescope diameter $D = 3.5$ m, sub-aperture diameter $D_{sub} = 0.15$ m, and separation between the LGSs is $\theta = 120\mu rad$. For Rayleigh beacons, the telescope diameter $D = 1$ m, sub-aperture diameter $D_{sub} = 0.1$ m, and separation between the LGSs is $\theta = 40\mu rad$. The focal length of the laser beam is $F = 30km$.

4. SENSITIVITY ANALYSIS

To evaluate the sensitivity of the slope cross-correlation to variations of the turbulence profile, we used the turbulence profile $C_n^2(z)$ models shown in Fig. 4. The slope cross-correlation coefficients were calculated from Eq. (6). Fig. 5 shows the slope cross-correlation coefficients for various turbulence profiles and Rayleigh LGSs. It is seen that the number of peaks of the cross-correlation coefficient corresponds to the number of the turbulent layers. The peaks position versus separation between the sub-apertures corresponds to the altitude of the turbulent layer, $H_i = r_i / \theta$. Variations of the cross-correlation coefficients caused by variations of the turbulence profile exceed the estimated measurement accuracy of the wavefront slope of 10%. Thus, the cross-path LIDAR technique has good sensitivity to variations of the turbulence profile.

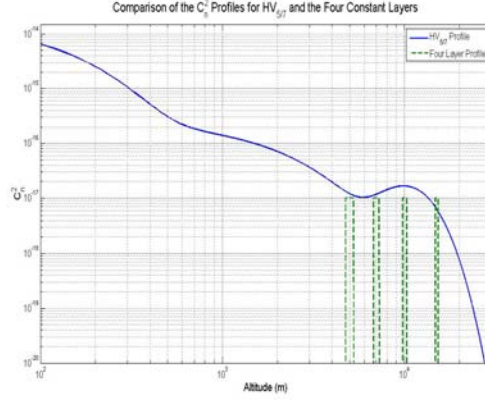


Fig. 4. Models of the turbulence profile $C_n^2(z)$ used in the analysis of the sensitivity of the cross-path LIDAR technique.

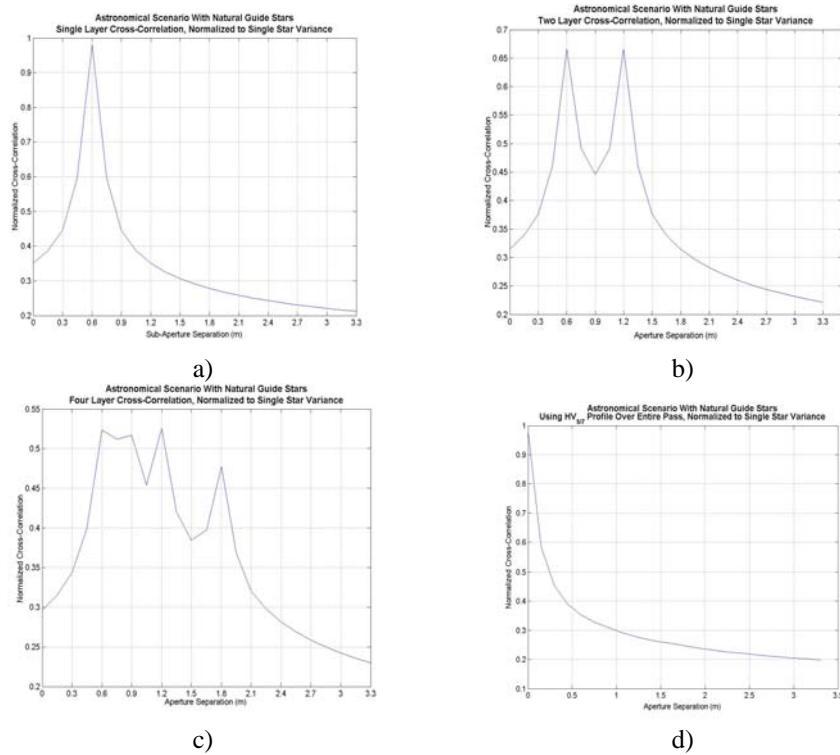


Fig. 5. Slope cross-correlation coefficients for various turbulence models for astronomical scenario using natural guide stars: a) single layer at 5 km altitude, b) two layers at 5 km and 10 km, c) four turbulent layers at 5 km, 7 km, 10 km, and 15 km, and d) HV_{57} turbulence model. The telescope diameter $D=3.5$ m, sub-aperture diameter $D_{\text{sub}}=0.15$ m, and separation between the natural GSs is $\theta=120\mu\text{rad}$.

5. PERFORMANCE ANALYSIS

The uncertainty in the measurement of an image centroid position due to photon statistics [12] is

$$\varepsilon = \frac{S_i}{SNR} \left(1 + \frac{N_B}{N_S} \right)^{1/2} \quad (9)$$

where ε is the rms of image centroid, S_i is the image spot diameter, N_S is the number of signal photons in the image, N_B is the number of sky background photons in the image, and SNR is the signal-to-noise ratio. Assuming a 4 pixel image spot size, the SNR is given by [13]

$$SNR = \frac{N_S}{\sqrt{N_S + 4(N_B + N_D + N_e^2)}} \quad (10)$$

where N_D is the number of dark current electrons per pixel and N_e is the number of read noise electrons per pixel. Figure 6 depicts the SNR for the cross-path LIDAR that uses a doubled frequency laser from Spectra Physics and low-noise CCD camera from Photometrics. The LIDAR is pointed at the zenith. It is seen that when the Rayleigh beacons altitude is lower than, or equal to, 17.5 km the signal-to-noise ratio is greater than ten. This suggests that a cross-path LIDAR using Rayleigh beacons is feasible.

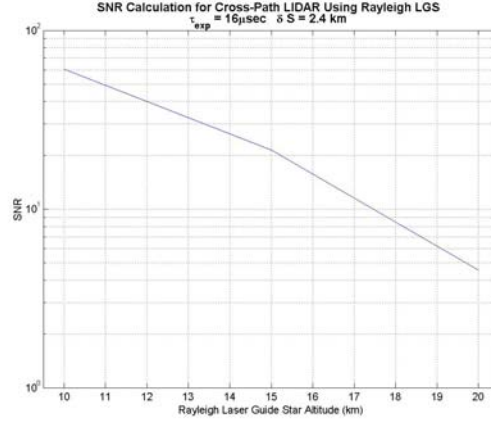


Fig. 6. The SNR for the cross-path LIDAR that uses a doubled frequency laser from Spectra Physics operating at 532 nm wavelength in conjunction with a low-noise CCD camera from Photometrics.

6. INVERSION ALGORITHM

Eq.(6) is Fredholm-type integral equation of the first kind with kernel $W(r_i, \theta, z)$. In this equation, $b(r_i, \theta)$ is the measured function, and $C_n^2(z)$ is the unknown function. A range-discrete version of Eq. (6) results in a matrix equation for calculating $C_n^2(z_j)$ values at discrete ranges z_j , $j = 1, \dots, n$, which has the form

$$b_i = \sum_{j=1}^n W_{ij} C_j + N_i \quad (11)$$

where $b_i = B(r_i, \theta) / B(0, 0)$, $C_j = C_n^2((j-1/2)\Delta z)$, $W_{ij} = \int_{(j-1)\Delta z}^{j\Delta z} W(r_i, \theta, z) dz$ and N_i is the measurement noise. Due to

the singular nature of the mathematical inversion procedure of the integral equation (11) of the first kind and the measurement noise, standard matrix inversion techniques are numerically unstable. Therefore, to retrieve the turbulence profile $C_n^2(z_j)$ from Eq. (11) a special-purpose inversion algorithm is required.

As a baseline approach for turbulence profile reconstruction, the Chahine iterative algorithm [14, 15] was selected. The basic idea of this method is to find the unknown function whose values when they are inserted into the Eq. (11) produce minimum deviation from the measured function $b(r_i, \theta)$. The procedure begins from selection of an initial guess for the turbulence profile. Once an initial guess $K_j^0 = [C_n^2(z_j)]^{(0)}$ is selected, we use this turbulence profile as

an input to Eq. (11) to calculate $\alpha_{cal}^0(r_i) = \sum_{j=1}^{n_s} K_j^0 W_{ij}$. The method performs multiple iterations to reduce the deviation from the measured function. If we denote the turbulence profile recovered after the n^{th} iteration as $K_j^n = [C_n^2(z_j)]^n$, and $\alpha_{meas}(r_i) = b(r_i, \theta)$ are the measured cross-correlation coefficients, then, first, for the turbulence profile K_j^n the estimates of the cross-correlation coefficient are calculated

$$\alpha_{cal}^n(r_i) = \sum_{j=1}^{n_s} K_j^n W_{ij} \quad (12)$$

and the turbulence profile is corrected as

$$K_j^{n+1} = K_j^n \frac{\alpha_{meas}(r_j)}{\alpha_{cal}^n(r_j)} \quad (13)$$

The convergence is estimated by calculating the root mean square residual error

$$\varepsilon = \left\{ \frac{1}{n_s} \sum_{i=1}^{n_s} \frac{[\alpha_{meas}(r_i) - \alpha_{cal}^n(r_i)]^2}{[\alpha_{cal}^n(r_i)]^2} \right\}^{1/2}, \quad (14)$$

where n_{sub} is the number of sub-apertures across the telescope aperture, as well as the number of ‘‘sensed’’ turbulence layers.

The reconstructed turbulence profiles using Chahine inversion algorithm [14, 15] for astronomical applications are shown below. Figure 7a depicts the original $HV_{5/7}$ turbulence profile, an initial guess, and reconstructed profiles that correspond to different numbers of iterations. It is seen that the reconstructed profile approaches the ‘‘true’’ profile by increasing the number of iterations, and the root mean square residual error is reduced. Figure 7b depicts an original profile, initial guess, and reconstructed profiles for various numbers of iterations for the step function $C_n^2(z_j)$ profile. When the number of iterations increases, the reconstructed turbulence profile approaches the original profile.

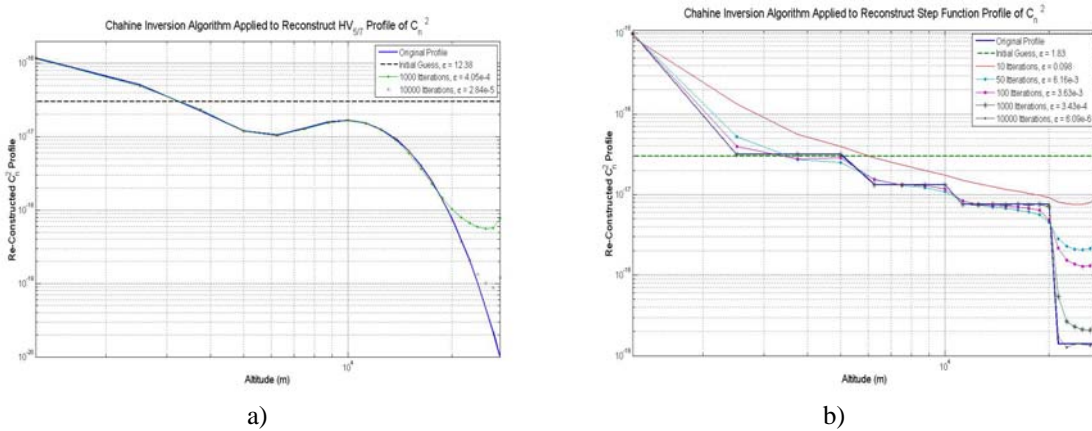


Fig. 7. The original $HV_{5/7}$ turbulence profile, an initial guess, and the reconstructed $C_n^2(z_j)$ profiles for different number of iterations (a). The original profile, initial guess, and reconstructed profiles for various numbers of iterations for the step function $C_n^2(z_j)$ profile (b)

Further analysis revealed that the reconstruction algorithm is robust with respect to measurement noise. However, the algorithm overestimates the thickness of the discrete turbulent layers. The reconstructed algorithm correctly

determines the number of layers, their altitudes, and maximum C_n^2 value in each layer. However, the thickness of the layers is overestimated.

To overcome this shortcoming, the reconstruction procedure was modified to include a rectangular fit to the reconstructed turbulence profile. The modified procedure includes two steps. First, the turbulence profile is reconstructed from the optical data using an iterative Chahine algorithm. Second, the reconstructed profile is approximated using a sum of rectangular functions

$$C_n^2(h) = \sum_{i=1}^n a_i \text{rect}\left(\frac{h-h_i}{b_i}\right) \quad (15)$$

where n is the number of turbulence layers, h_i is the layer altitude, and b_i is the thickness of the layer, and a_i is the strength of turbulence within the layer. Four parameters of the rectangular fit to the reconstructed turbulence profile are determined sequentially. First, the number of turbulence layers is determined using a threshold. Then the altitude and the thickness of the layers are determined from the C_n^2 values above the threshold. Third, the strength of

turbulence is estimated from the integral values of C_n^2 for each layer. Finally, the total integral $\mu_{rec} = \int_0^{H_{max}} C_n^2(h) dh$ estimated from the rectangular fit to the reconstructed turbulence profile is compared to the measured value of this

integral $\mu_0 = \int_0^{H_{max}} C_n^2(h) dh$, which is retrieved from the variance of the slope, or differential slope, measurements for

a single LGS. Two examples of reconstructed turbulence profiles “measured” using Rayleigh beacons at 15 km altitude are shown in Fig. 8. The reconstructed profiles are close to the original profiles. This validates the proposed approach.

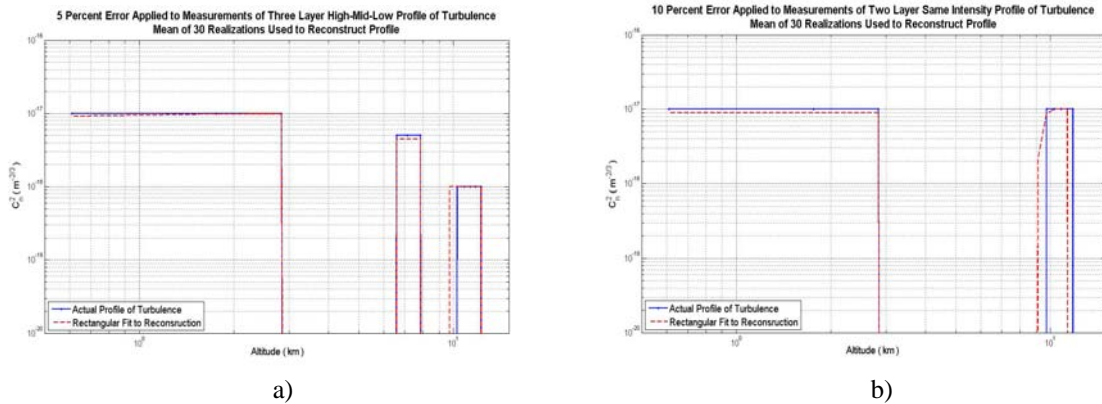


Fig. 8a and b. Comparison of the reconstructed turbulence profiles with original profiles. The rms measurement error is 5% and 10% for a), and b), respectively. Blue line corresponds to the original profile. Red line depicts the reconstructed turbulence profile using Chahine iterative algorithm combined with edge detection algorithm and rectangular fit.

7. CONCLUSIONS

In the study the following results were obtained:

- The analytical model for the cross-path LIDAR was developed and validated using wave-optics simulation code. We found that the analytical model is accurate and agrees well with predictions from the wave-optics code
- The sensitivity of the cross-correlation coefficients of the wavefront slopes to variations of the turbulence profile was evaluated. It was found that the cross-correlation coefficient of a wavefront slope is highly sensitive to variations of the turbulence profile

- The inversion algorithm for reconstruction of the turbulence profile was developed and tested in simulation. We found that the algorithm is accurate and robust to measurement noise
- Performance analysis of the cross-path LIDAR was performed. We found that a field demonstration of the cross-path LIDAR is feasible. We also found that a doubled frequency laser from Spectra Physics operating at 532 nm wavelength in conjunction with the CCD camera from Roper Scientific provide the best performance
- We showed the cross-path LIDAR is able to measure three atmospheric characteristics: turbulence profile, turbulence outer scale, and wind velocity from which two wave propagation parameters including Fried parameter and Greenwood frequency can be calculated [10].

8. ACKNOWLEDGMENTS

This work was funded by the U. S. Air Force Phase I SBIR under contract FA9451-05-M-0064. The authors greatly acknowledge their support.

9. REFERENCES

1. F. Eaton, B. Balsley, R. Frehlich, R. Hugo, M. Jensen, and K. McCrae, "Turbulence observations over a desert basing using a kite/tethered-blimp platform," *Optical Engineering*, Vol. 39, 2517-2526(2000)
2. F. Eaton, P. Kelly, D. Kyrakis, and J. Ricklin, "Impact of realistic turbulence conditions on laser beam propagation," *Proc. SPIE*, Vol. 5550, 267-274(2004)
3. F. D. Eaton, W. A. Peterson, J. R. Hines, J. J. Drexler, A.H. Waldie and D. B. Soules, "Comparison of two techniques for determining atmospheric seeing," *Proc. SPIE*, Vol. 926, 319-334(1988)
4. R. Avila, J. Vernin, and E. Masciadri, "Whole atmospheric-turbulence profiling with generalized SCIDAR," *Appl. Opt.*, Vol. 36, 7898(1997)
5. V. A. Kluchers, N. J. Wooder, T. W. Nicholls, M. J. Adcock, I. Munro, and J. C. Dainty, "Profiling of atmospheric turbulence strength and velocity using a generalized SCIDAR technique," *Astronomy and Astrophysics*, Vol. 335 (1), 1998
6. J. L. Prieur, C. Daigne, and R. Avila, "SCIDAR measurements at Pic du Midi," *Astronomy and Astrophysics*, Vol. 371, 366-377 (2001)
7. M. S. Belen'kii, D. W. Roberts, J. M. Stewart, G. G. Gimmestad, and W. R. Dagle, "Experimental validation of the differential image motion lidar technique," *Optics Letters*, Vol. 25, 518-520(2000)
8. R. W. Wilson, "SLODAR: measuring optical turbulence altitude with a Shack-Hartmann wavefront sensor," *Mon. Not. R. Astron. Soc.*, Vol. 337, 103-108(2002)
9. B. Ellerbroek, "Estimating turbulence statistics as a step in PSF reconstruction for LGS MCAO" HIA workshop on PSF Reconstruction, AURA New Initiative Office, May 12, (2004)
10. M. Belen'kii, D. Bruns, E. Korevaar, K. Hughes, and V. Rye, "Optical Methods for Turbulence Profile Determination," Final Report AFRL-DE-PS, TR-2005-XXXX, (2005)
11. V. I. Tatarskii, *Wave Propagation in a Turbulence medium*, (McGraw-Hill, New York, 1961).
12. J. S. Morgan, D. C. Slater, J. G. Timothy, and E. B. Jenkins, "Centroid position measurements and subpixel sensitivity variations with the MAMA detector," *Appl. Opt.*, Vol. 28, 1178-1192(1989)
13. R. Fugate, "Laser beacon adaptive optics for power beaming applications," *SPIE Proc.*, Vol. 2121, 68-76(1994).
14. M. T. Chahine, "Determination of the temperature profile in an atmosphere from its outgoing radiance," *JOSA A*, Vol. 58, 1634-1637(1968)
15. M. T. Chahine, "Inverse problems in radiative transfer: determination of atmospheric parameters," *J. Atmos. Sci.*, Vol. 27, 960-967(1970))